

# Gasochromic $\text{WO}_3/\text{MoO}_3$ sensors prepared by co-sputtering for hydrogen leak detection with long-lasting visible signal

Chiwan Park <sup>a</sup>, Seung-Ik Han <sup>a,b</sup>, Le Thai Duy <sup>c,d</sup>, Rubaya Yeasmin <sup>a,b</sup>, Gwanggyo Jung <sup>a</sup>, Dong Won Jeon <sup>a</sup>, Woongchan Kim <sup>a</sup>, Sung Beom Cho <sup>a,e</sup>, Hyungtak Seo <sup>a,e,\*</sup>

<sup>a</sup> Department of Energy Systems Research, Ajou University, Suwon 16499, Republic of Korea

<sup>b</sup> Engineering Research Institute, Ajou University, Suwon 16499, Republic of Korea

<sup>c</sup> Faculty of Materials Science & Technology, University of Science, Ho Chi Minh City 70000, Viet Nam

<sup>d</sup> Vietnam National University (VNU), Ho Chi Minh City 70000, Viet Nam

<sup>e</sup> Department of Materials Science and Engineering, Ajou University, Suwon 16499, Republic of Korea



## ARTICLE INFO

### Keywords:

Tungsten oxide  
Molybdenum oxide  
Gasochromic  
Irreversible  
Hydrogen sensors

## ABSTRACT

Hydrogen is a renewable energy resource used as a fuel carrier with many advantages for future hydrogen economy systems. However, the safety of handling hydrogen fuel is of great concern due to explosion risks. Thus, in this study, a cost-effective  $\text{WO}_3/\text{MoO}_3$ -based gasochromic hydrogen sensor having a long-lasting signal (i.e., irreversible color change) is developed for detecting hydrogen leaks. Particularly, the active  $\text{WO}_3/\text{MoO}_3$  compound film is deposited on a glass substrate by co-sputtering, and an ultrathin Pd catalyst layer for hydrogen gas decomposition is deposited on it using e-beam evaporation. Various characterizations are conducted to understand the structural, chemical, and optical properties of the  $\text{WO}_3/\text{MoO}_3$ -Pd films. In general, our  $\text{WO}_3/\text{MoO}_3$ -Pd sensor has excellent gas discoloration starting from 0.1 % of hydrogen concentration (in dry air) with fast response speed at room temperature. Besides, a DFT study further explains the sensing mechanism of our hybrid  $\text{WO}_3/\text{MoO}_3$  structure. Those highlight the potential of our developed sensor for practical hydrogen sensing applications.

## 1. Introduction

Hydrogen sensors are classified based on their operating principles [1], such as catalytic [2–4], semiconductor [5], electrochemical [6], resistive [7–10], and chromogenic-based sensors [11]. Each sensor type is selected depending on specific environmental conditions and requirements. Among them, resistive-based sensors are useful for applications demanding high sensitivity and diverse gas detection capabilities. However, they require electrical power to operate and have a complex structure, resulting in higher manufacturing and maintenance costs, making them less feasible for widespread deployment. In contrast, chemochromic sensors offer a simple and flexible structure, making them cost-effective and suitable for complementing the advantages and disadvantages of electrical sensors when used together. Hydrogen chemochromic sensors are operated by its color change due to their interaction with hydrogen. Leveraging this characteristic, hydrogen chemochromic sensors find diverse applications across various fields, particularly in environmental monitoring, medical, and industrial

process control [12]. These sensors play a crucial role in hydrogen detection and analysis, as hydrogen is an important energy source but poses explosion risks when accumulated in high concentrations [13–15]. Thus, accurate detection of hydrogen leaks is vital for enhancing safety and energy efficiency.

Various materials can be used in hydrogen chemochromic sensors, with notable examples being  $\text{WO}_x$  [11,16–20],  $\text{MoO}_x$  [21–25],  $\text{VO}_x$  [26, 27],  $\text{TiO}_2$  [8,28,29] etc. Transition metal oxides (TMOs) [30–32] like  $\text{WO}_3$  and  $\text{MoO}_3$  offer advantages in sensitivity, selectivity, and stability. These properties provide high detection sensitivity, making them suitable for rapid hydrogen detection and the development of alarm systems. Particularly,  $\text{WO}_3$  or tungsten trioxide is one of the most common materials used in hydrogen-sensitive sensors [11,33,34].  $\text{WO}_3$ -based hydrogen sensors can detect the concentration of hydrogen in the atmosphere by exhibiting a change in optical properties, specifically a dark blue color shift at certain wavelengths as the hydrogen concentration increases. These optical characteristics of  $\text{WO}_3$  change when it interacts with hydrogen in air. Furthermore,  $\text{WO}_3$  possesses a reversible

\* Corresponding author at: Department of Energy Systems Research, Ajou University, Suwon 16499, Republic of Korea

E-mail address: [hseo@ajou.ac.kr](mailto:hseo@ajou.ac.kr) (H. Seo).

color-changing property, meaning that upon the decrease in hydrogen concentration, it can return to its original state, restoring its green color [11,33,34]. On the other hand, MoO<sub>3</sub>-based hydrogen sensors operate on a similar principle to WO<sub>3</sub>-based sensors but exhibit an irreversible color-changing behavior; As the hydrogen concentration increases, the color of MoO<sub>3</sub> changes, and its transparency decreases. However, the color of MoO<sub>3</sub> does not fully return to its initial state even if hydrogen exposure is decreased, and some long-lasting changes persist.

By utilizing the characteristics of WO<sub>3</sub> and MoO<sub>3</sub>, hybrid WO<sub>3</sub>/MoO<sub>3</sub>-Pd hydrogen sensors are promising to leverage the beneficial properties of both materials to enhance reactivity and selectivity. This combination offers improved performance in hydrogen detection and various gas detection applications. The rapid response characteristic of WO<sub>3</sub> enables it to undergo a color change in response to varying hydrogen concentrations quickly. In contrast, the MoO<sub>3</sub> irreversible behavior contributes to the sensor maintaining a certain level of color change even after the hydrogen concentration decreases. The theoretical explanation for why the transmittance of WO<sub>3</sub> and MoO<sub>3</sub> changes when they interact with hydrogen is still an area of active research, and a complete understanding has not yet been achieved. However, the polaron theory is commonly proposed as one possible mechanism to explain the interaction between hydrogen and WO<sub>3</sub>/MoO<sub>3</sub>-Pd [35]. To gain more accurate understanding, further research is required in this area.

Herein, our development of hybrid WO<sub>3</sub>/MoO<sub>3</sub>-Pd hydrogen sensors is introduced. The hydrogen sensing ability of this hybrid material was investigated by experimental and theoretical approaches. The proposed WO<sub>3</sub>/MoO<sub>3</sub>-Pd sensor has excellent gas discoloration starting from 0.1 % of hydrogen concentration (in dry air) with fast response speed at room temperature, the mechanism of which is explained by bond strength differentiation between hydrogen and cations (W or Mo) in metal oxides.

## 2. Experimental

### 2.1. Deposition of WO<sub>3</sub>/MoO<sub>3</sub>-Pd thin film

The thin films were fabricated using an RF magnetron sputtering system (13.56 MHz, Sci & Tech, Korea) with WO<sub>3</sub> (99.95 %) and MoO<sub>3</sub> (99.95 %) (TIPAIN, Korea) targets. The deposition was carried out at 10 mTorr process pressure with an Ar flow rate of 30 sccm and an applied voltage of 150 W at room temperature, resulting in films with approximately 700 nm of thickness on glass substrates (Sigma Aldrich, USA) and SiO<sub>2</sub> wafers (Waferbiz, Korea). Co-sputtering was employed to create a mixture of WO<sub>3</sub> and MoO<sub>3</sub> having a ratio of WO<sub>3</sub>:MoO<sub>3</sub> ≈ 2:1. The mixture ratio of as deposited WO<sub>3</sub>/MoO<sub>3</sub> sensor layer was further confirmed by EDS elemental mapping, as explained in Section 3.1. The mixture deposition process followed the same conditions as the single-film deposition: process pressure of 10 mTorr, Ar flow rate of 30 sccm, and applied voltage of 150 W. Pd was used as a hydrogen dissociation catalyst and was deposited using an e-beam evaporator (Sci & Tech, Korea). The thickness of the catalyst layer was set at 4 nm for all samples, and it was slowly deposited at a rate of 1.0 Å s<sup>-1</sup> under a base pressure of  $3 \times 10^{-6}$  Torr. In this fabrication method, thin films of WO<sub>3</sub>/MoO<sub>3</sub>-Pd were deposited on four (4) glass substrates (of width = 2.5 cm, and length = 7.5 cm) at the same time. Finally, the glass substrates with WO<sub>3</sub>/MoO<sub>3</sub>-Pd sensing layer were cut into small pieces that gives a total of 12 samples, having a sensing area of 2.5 x 2.5 cm<sup>2</sup>, in one batch. Unless specified otherwise, the above-mentioned samples, having a sensing area of 2.5 x 2.5 cm<sup>2</sup>, were used in the gasochromic sensing experiments. It should be noted that the samples can be cut into smaller pieces than that of 2.5 x 2.5 cm<sup>2</sup> to get more samples out of one batch, and samples of all size perform effectively irrespective to their size/sensing area.

### 2.2. Characterization and measurements

Various methods were employed to analyze the samples' structural, optical, electrical, and chemical properties. Surface and cross-sectional morphologies and elemental mapping of the films were observed with a scanning electron microscope (FE-SEM, JSM-6700F, JEOL, Japan). X-ray diffraction data were acquired using a high-resolution X-ray diffractometer (Ultima III, Rigaku, Japan), where Cu-Kα X-ray source was used. The chemical bonding states of WO<sub>3</sub> and MoO<sub>3</sub> were measured using X-ray photoelectron spectroscopy (XPS) with a Nexus XPS (Thermo Fisher Scientific, USA). The bonding characteristics of WO<sub>3</sub> were investigated through Raman spectroscopy (LabRam HR Evolution, HORIBA Jovin Yvon, France). Molecular vibrations of water were probed using Fourier-Transform Infrared Spectroscopy (FTIR) on a Nicolet iS50 instrument (Thermo Fisher Scientific, USA). Color changes were monitored using a UV-visible system from AVANTES (Detector: AvaSpec-ULS2048, Light source: AvaLight-DH-S-BAL). Real-time color changes were quantified using the color difference ( $\Delta E$ ) method (AvaSoft 8.0, AVANTES) based on changes in transmittance before and after H<sub>2</sub> exposure and over time. The value of  $\Delta E$  is calculated using the following equation:  $\Delta E = [(L-L')^2 + (a-a')^2 + (b-b')^2]^{1/2}$ . Where, L, a, and b indicate the lightness value, position on the red-green axis, and position on the yellow-blue axis, respectively of the sample before gas exposure. The same parameters with prime (') indicate the same properties after gas exposure [17].

Here, the gas sensing measurements were performed using the mass flow controller (MFC) operated small chamber system (NEXTRON). For H<sub>2</sub> sensing performance evaluation, commercially available hydrogen bottles of different concentrations (0.1 %, 4 %, and 10 % H<sub>2</sub>) were employed. In addition, different bottles of noise gas such as NH<sub>3</sub> (10 %), NO (1000 ppm), CH<sub>4</sub> (10 %), CO (1000 ppm), NO<sub>2</sub> (1000 ppm), CO<sub>2</sub> (1000 ppm), and C<sub>2</sub>H<sub>5</sub>OH (10 %) were used for the selectivity test. Gas concentration, exposure time, and flow rate of target gases were controlled by the MFC. The total flow rate was maintained at 500 sccm during all the sensing measurements inside chamber. All the gas sensing measurements were performed in dry air, except for the humidity test (where humid H<sub>2</sub> flow was introduced using a bubbler). The humidity injection rate through the bubbler was controlled by MFC, and the relative humidity as well as operating temperature inside the chamber was measured by a hygrometer (CEM DT-616CT).

### 2.3. Density functional theory calculation

All the density functional theory (DFT) calculations were carried out utilizing the Vienna ab-initio simulation package (VASP) [36]. The calculations are performed using the projector-augmented wave method [37], and the exchange-correlation potential was described by the generalized gradient approximation (GGA) [38] within the Perdew-Burke-Ernzerhof (PBE) parameterization. An energy cut-off of 520 eV was chosen to minimize the Pulay stress during the calculations. The k-points were systematically sampled with a minimum density of 1000 points / nm<sup>3</sup> to ensure precision in all DFT calculations.

The atomic structure of WO<sub>3</sub>/MoO<sub>3</sub> for the DFT calculations was constructed based on the WMoO<sub>6</sub> configuration available in the materials project database [39]. The configuration was duplicated to create a 2x2x2 supercell containing 128 atoms. The solid-solution alloy model was generated by an ensemble approach with random substitution of W and Mo atoms in accordance with the desired ratio, utilizing the VASPKIT software [40]. This alloy model was geometrically optimized through iterative DFT calculations. The amorphous structures were constructed via two-step methods. Molecular dynamics (MD) simulations were first performed employing universal machine-learned atomistic models such as CHGnet [41]. The process involved initially heating the cells beyond their melting point to erase the original crystalline arrangement [42,43]. Subsequently, the structures were heated close to their melting points, followed by rapid quenching. To achieve system

equilibrium, at least 70 ps MD simulation at room temperature was executed. Finally, the structures were sampled and relaxed to 0 K to attain their respective ground states via DFT.

### 3. Results and discussion

#### 3.1. Characterization of $\text{WO}_3/\text{MoO}_3\text{-Pd}$

**Fig. 1(a)** shows the fabrication process of our  $\text{WO}_3/\text{MoO}_3$  samples using co-sputtering of  $\text{WO}_3$  and  $\text{MoO}_3$  at a low temperature. After co-sputtering of  $\text{WO}_3$  and  $\text{MoO}_3$ , an ultrathin Pd layer was deposited on the sample as a catalyst for activating reactions with hydrogen gas. **Fig. 1(b)** explains the roles of each layer in detecting hydrogen. In the literature, hydrogen gas can be dissociated on Pd surface into hydrogen atoms (i.e., spill-over effect [44]). Then, hydrogen atoms will bind to oxygen in the lattice of  $\text{MoO}_3$  and  $\text{WO}_3$ , as expressed in Equations (1) and (2), in which  $\text{MO}_3$  is presenting for  $\text{WO}_3$  and  $\text{MoO}_3$ . That finally results in a reduction in oxidation states of  $\text{WO}_3$  and  $\text{MoO}_3$  which would cause their color change (i.e., gasochromic effect).



The morphological characterization of the  $\text{WO}_3/\text{MoO}_3$  thin films deposited on  $\text{SiO}_2$  substrates were investigated, as shown in **Fig. 2**. Here, SEM images in **Fig. 2(a)** shows the surface morphology and thickness profile (inset image shows the 600-nm-thick film) of our prepared  $\text{WO}_3/\text{MoO}_3$  sensor.

$\text{MoO}_3$  sample. The formation of nano-cracks on the surface of  $\text{WO}_3/\text{MoO}_3$  film confirms the porosity of our prepared  $\text{WO}_3/\text{MoO}_3$  sample, allowing gas/air to enter and move inside the layer that promote the adsorption of hydrogen molecules and enhance reactivity. This nano-cracked porosity is an important feature that can improve the sensitivity and response rate of the hydrogen sensor. In **Fig. 2(b)**, the chemical composition of the  $\text{WO}_3/\text{MoO}_3$  thin film was analyzed using energy dispersive X-ray spectroscopy (EDS). The EDS and elemental distribution shown an elemental ratio of  $\text{W:Mo} \approx 2:1$  and thus, indicates the formation of  $\text{WO}_3/\text{MoO}_3$  sensor layer having a mixture ratio of  $\text{WO}_3:\text{MoO}_3 \approx 2:1$ . Although the  $\text{WO}_3$  and  $\text{MoO}_3$  films were deposited under the same co-sputtering conditions,  $\text{MoO}_3$  (target) has a higher elastic modulus than  $\text{WO}_3$  (target) (ca. 540 GPa vs. 150–450 GPa, respectively) [44], resulting in the content of W in the mixed film higher than that of Mo. This result is also in good agreement with the structural characterization performed by X-ray diffractometer (XRD), as shown in **Figure S1 (in Supplementary Information)**.

**Figure S1 (in Supplementary Information)** presents the XRD patterns of  $\text{WO}_3$  (black line),  $\text{MoO}_3$  (blue line), and  $\text{WO}_3/\text{MoO}_3$  (red line) films having similar total deposition time. The XRD pattern of bare  $\text{WO}_3$  with main characteristic peaks (at  $2\theta = \text{ca. } 30^\circ, 47^\circ, 54^\circ$ , and  $56^\circ$  corresponding to the crystal planes (200), (002), (221), and (311), respectively) presents the hexagonal  $\text{WO}_3$  phase, which coincide with JCPDS-75-2187 [45]. The diffraction pattern of bare  $\text{MoO}_3$  perfectly matched with hexagonal  $\text{MoO}_3$  phase (JCPDS-21-05690), where the characteristic peaks are attributed to the crystal planes (100), (110), (200), (210), (300), (310), (404), and (218), respectively [45,46]. In the

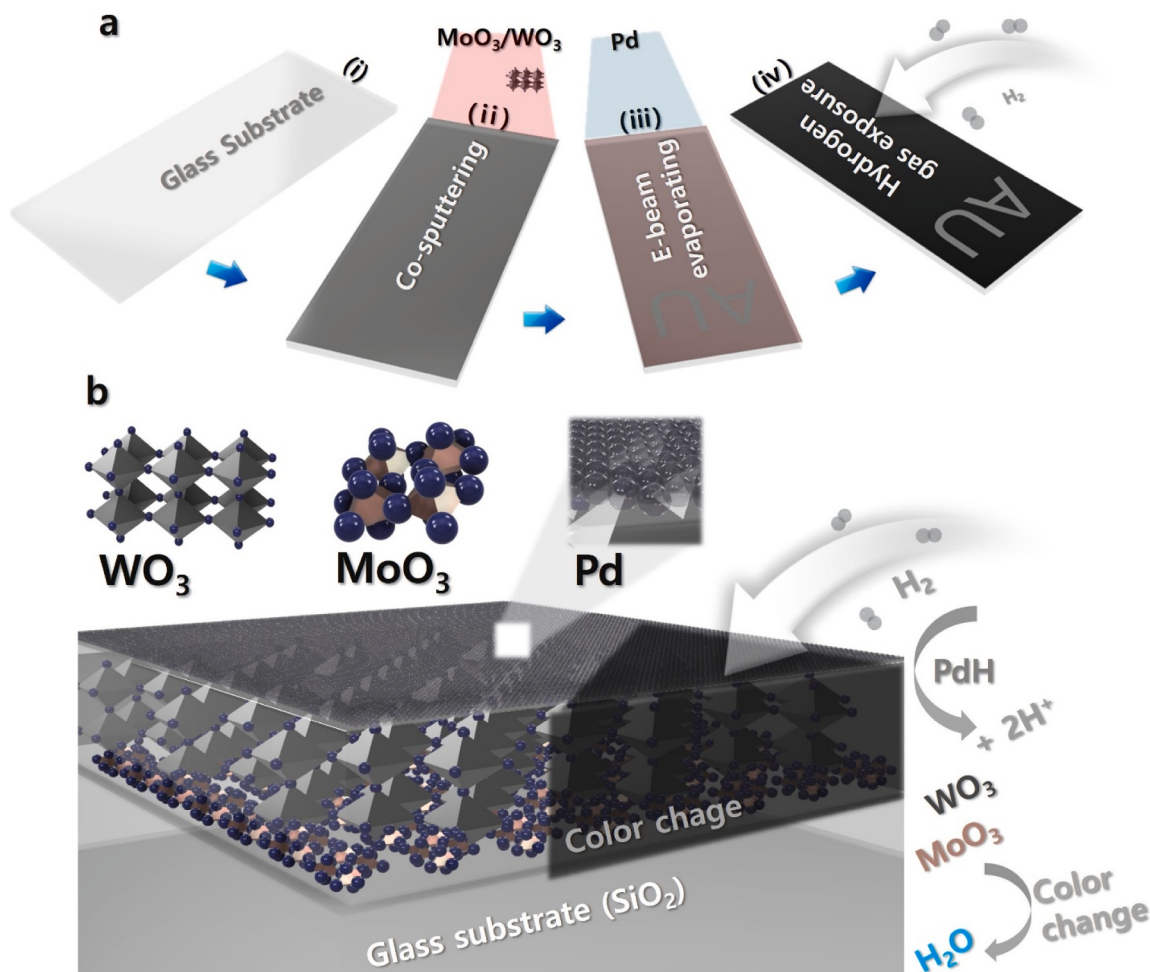


**Fig. 1.** (a) Overall fabrication process and hydrogen sensing characteristics of hydrogen sensor. Deposition of  $\text{WO}_3$  and  $\text{MoO}_3$  using co-sputtering and deposition of Pd using E-beam evaporator were performed on a glass substrate. (b) Structure and reaction mechanism of the fabricated  $\text{WO}_3/\text{MoO}_3\text{-Pd}$  sensor.

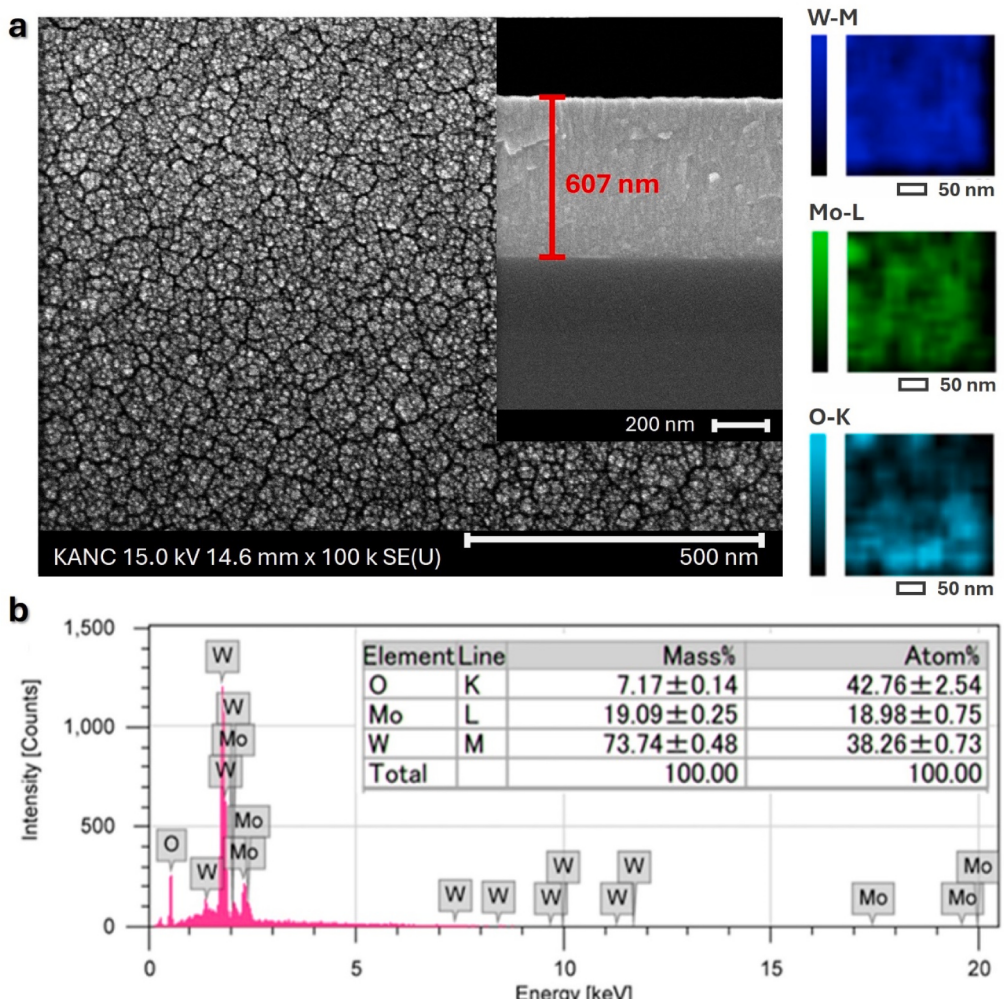


**Fig. 2.** Morphological property. (a) Surface and cross-sectional FE-SEM images of an as-deposited  $\text{WO}_3/\text{MoO}_3$  film. The  $\text{WO}_3/\text{MoO}_3$  film shows a porous structure and a vertical nanocolumn structure with a thickness of about 600 nm. (b) Cross-sectional EDS mapping and elemental distribution, respectively of the  $\text{WO}_3/\text{MoO}_3$  film.

case of XRD pattern of composite ( $\text{WO}_3/\text{MoO}_3$ ) sample, there is an overall similarity in the peak positions to that of bare  $\text{WO}_3$  sample, which is due to the relatively low amount of Mo (than that of W) in the composite sample [47]. This is also consistent with the results from EDS elemental mapping and Raman spectroscopy as shown in Figs. 2b, and 4(c), respectively. Nevertheless, the  $\text{WO}_3/\text{MoO}_3$  film consists of the major amorphous phase and minor crystal phase, as evidenced by the appearance of tiny characteristic peaks in the XRD pattern of  $\text{WO}_3/\text{MoO}_3$  film in Figure S1. Regardless of the minor crystal phase, the nano-cracked structures of  $\text{WO}_3/\text{MoO}_3$  films (having abundant surface areas, containing more defect sites) allow more gas adsorption and chemical reactions.

For further understanding of the film's chemical composition, X-ray photoelectron spectroscopy (XPS) measurements were performed with Al  $\text{K}\alpha$  X-ray source employed for the analysis of the chemical state of three oxide films. Besides, the C1s peak were calibrated at a binding energy of 284.6 eV. Fig. 3(a,b) shows the comparison of the W 4 f peak before and after 4 %  $\text{H}_2$  exposure for the  $\text{WO}_3\text{-Pd}$  film. In its initial state, the  $\text{WO}_3\text{-Pd}$  film consists mainly two oxidation states, such as  $\text{W}^{6+}$  (at 38.2 eV in the 4  $f_{5/2}$  peak and at 36.1 eV in the 4  $f_{7/2}$  peak) and  $\text{W}^{5+}$  (at 36.8 eV in the 4  $f_{5/2}$  peak and at 34.7 eV in the 4  $f_{7/2}$  peak) [48]. After exposure to 4 %  $\text{H}_2$ , the XPS measurement of the recovered sample revealed a reversible nature, as it returned to a state almost identical to its initial condition. Fig. 3(c,d) presents the results of the Mo 3d peak measurement for the  $\text{MoO}_3\text{-Pd}$  film. Mo exhibits 3 major oxidation

states, such as  $\text{Mo}^{6+}$  (in 3d<sub>5/2</sub>: 232.4 eV, and in 3d<sub>3/2</sub>: 235.8 eV),  $\text{Mo}^{5+}$  (in 3d<sub>5/2</sub>: 230 eV, and in 3d<sub>3/2</sub>: 234.6 eV), and  $\text{Mo}^{4+}$  (in 3d<sub>5/2</sub>: 229.2 eV, and in 3d<sub>3/2</sub>: 232.4 eV) [49]. Upon exposure to 4 %  $\text{H}_2$ , hydrogen interacts with oxygen atoms, forming water molecules and creating oxygen vacancies, which affect the intensity of the Mo oxidation state; as a result,  $\text{Mo}^{6+}$  peak decreased while the  $\text{Mo}^{5+}$  and  $\text{Mo}^{4+}$  peaks increased, indicating an irreversible behavior where the oxidation state of Mo was maintained even in a non-hydrogen or air (after the hydrogen exposure ended). In general, we found that after hydrogen sensing test, the W binding states of  $\text{WO}_3\text{-Pd}$  would recover to the initial state while the Mo binding states of  $\text{MoO}_3\text{-Pd}$  would remain for a long period, more than 24 hrs. Interestingly, after two oxides were mixed together, the recovery of the W binding states of  $\text{WO}_3/\text{MoO}_3\text{-Pd}$  was extensively reduced, as revealed in Fig. 3(e,f). Before hydrogen exposure, the  $\text{WO}_3/\text{MoO}_3\text{-Pd}$  sample showed a similar pattern to the  $\text{WO}_3\text{-Pd}$  film. However, the  $\text{WO}_3/\text{MoO}_3\text{-Pd}$  sample after 4 %  $\text{H}_2$  exposure and subsequent air aging for 24 hrs exhibited that the decreased intensity of the  $\text{W}^{6+}$  peak and the increased intensity of the  $\text{W}^{5+}$  peak were differentiated from those of the initial sample (before hydrogen exposure). This indicate that the  $\text{WO}_3$  component in the composite oxide film exhibits the same irreversible behavior as the  $\text{MoO}_3$  component. Altogether, the XPS analysis provided valuable insights into the chemical states of our mixed  $\text{WO}_3/\text{MoO}_3\text{-Pd}$  film and revealed their reversible-to-irreversible transition behaviors after hydrogen exposure, which is crucial for understanding the properties and potential

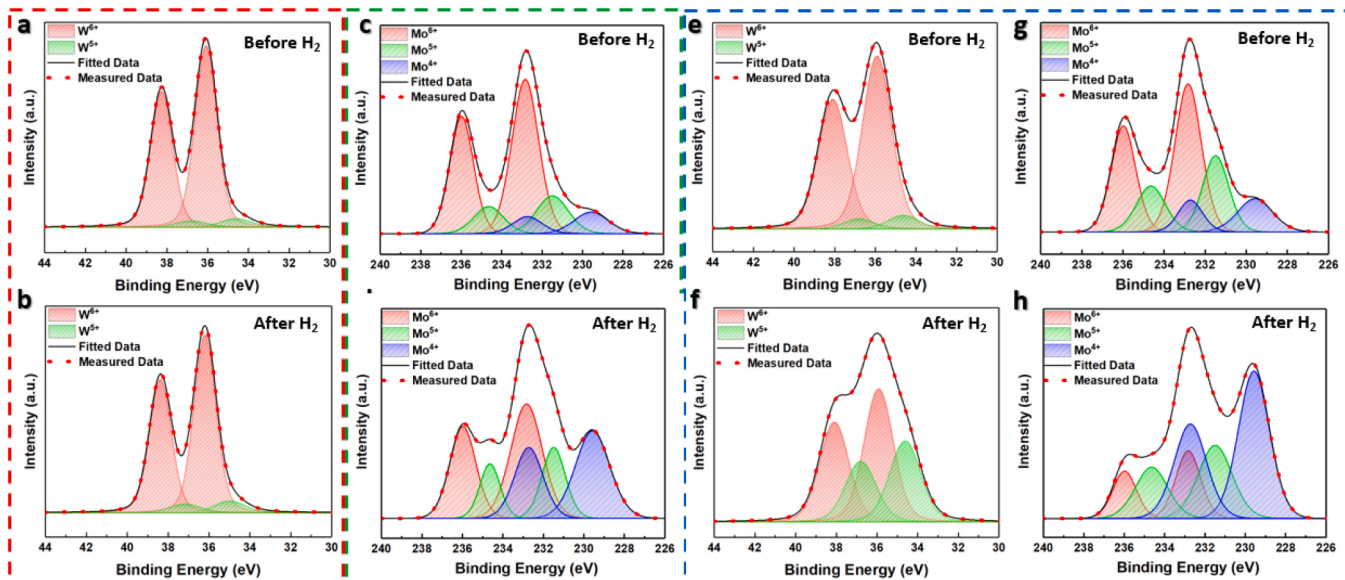


**Fig. 3.** XPS Characteristics of  $\text{WO}_3\text{-Pd}$ ,  $\text{WO}_3/\text{MoO}_3\text{-Pd}$  Films. (a, b)  $\text{W} 4\text{f}$  peak spectrum of  $\text{WO}_3\text{-Pd}$  single film before and after 4 %  $\text{H}_2$  exposure. (c, d)  $\text{Mo} 3\text{d}$  peak spectrum of  $\text{MoO}_3\text{-Pd}$  single film before and after 4 %  $\text{H}_2$  exposure. (e, f)  $\text{W} 4\text{f}$  peak spectrum of  $\text{WO}_3/\text{MoO}_3\text{-Pd}$  film before and after 4 %  $\text{H}_2$  exposure. (g, h)  $\text{Mo} 3\text{d}$  peak spectrum of  $\text{WO}_3/\text{MoO}_3\text{-Pd}$  film before and after 4 %  $\text{H}_2$  exposure.

applications of these films in hydrogen sensors. Furthermore, the XPS analysis verified the proposed hydrogenation mechanism.

To collect further information regarding the formation of products (such as -OH and  $\text{H}_2\text{O}$ ) after reactions illustrated in Eqs. (1) and (2), Fourier-transform infrared (FT-IR) spectroscopic and Raman spectroscopic measurements were performed and summarized in Fig. 4. In Fig. 4(a), it was observed that the FT-IR intensity of  $\text{WO}_3/\text{MoO}_3\text{-Pd}$  decreased compared to individual monolayers of  $\text{WO}_3\text{-Pd}$  and  $\text{MoO}_3\text{-Pd}$ , and a distinct peak corresponding to surface O-H stretching in the range of  $3000\text{--}3500\text{ cm}^{-1}$  was observed in the  $\text{WO}_3$ -containing films [50]. This difference further increased upon encountering 4 %  $\text{H}_2$ , indicating the incorporation of a significant amount of  $\text{H}_2\text{O}$  through hydrogen binding. This observation was consistent with the results from XPS analysis in Fig. 3, where variations in  $\text{W}^{6+}$  and  $\text{W}^{5+}$  peak intensities were noted. Additionally, in the  $1400\text{--}1700\text{ cm}^{-1}$  range corresponding to O-H bending [50], similar evidence of hydrogen incorporation was observed. Fig. 4(c,d) shows the Raman results of those films. As shown here, the Raman spectrum of the  $\text{WO}_3/\text{MoO}_3\text{-Pd}$  film was similar to that of the  $\text{WO}_3\text{-Pd}$  film because the portion of W in the film was twice that of  $\text{MoO}_3\text{-Pd}$ . Upon exposure to 4 %  $\text{H}_2$ , new peaks at  $330$  and  $450\text{ cm}^{-1}$  appeared in  $\text{WO}_3/\text{MoO}_3\text{-Pd}$ , which are associated with the vibrations of  $\text{O}-\text{W}^{5+}-\text{O}$  and  $\text{W}^{5+}=\text{O}$  bonds[51]. When hydrogen ions and electrons are inserted into  $\text{WO}_3$  films, electrons reduce  $\text{W}^{6+}$  ions to  $\text{W}^{5+}$ . This is consistent with the results of changes in the  $\text{W}^{6+}$  and  $\text{W}^{5+}$  peak intensities in the XPS analysis in Fig. 3.

### 3.2. Gasochromic performances

UV-Vis measurements were performed at room temperature to quantify the visible color changes of  $\text{WO}_3/\text{MoO}_3\text{-Pd}$  films (on glass substrates) before and after 4 % hydrogen exposure (4 %  $\text{H}_2$  in  $\text{N}_2$  balance). Fig. 5(a-c) shows the overall transmittance change in the range of  $300\text{--}1000\text{ nm}$  of wavelength when each hydrogen sensor was exposed to 4 %  $\text{H}_2$  for 1 min and then, no  $\text{H}_2$  exposure was held (i.e., declared as final change) until the lowest saturation of transmittance is reached before introducing air-purging. The  $\text{MoO}_3\text{-Pd}$  sensor in Fig. 5(a) exhibited a lower rate of change compared to the  $\text{WO}_3\text{-Pd}$  in Fig. 5(b) and  $\text{WO}_3/\text{MoO}_3\text{-Pd}$  sensors in Fig. 5(c). At 700 nm, the  $\text{MoO}_3\text{-Pd}$  sensor had an initial transmittance of 47.43 %, which decreases to 28.82 % after 1 min of 4 % hydrogen exposure, with a final change of 5.55 %.

The  $\text{WO}_3\text{-Pd}$  sensor had an initial transmittance of 57.14 % and showed a dramatic reduction of transmittance to 17.83 % with 4 %  $\text{H}_2$  for 1 min. Especially, significant changes were observed mainly in the long-wavelength region, indicating that  $\text{WO}_3$  turned dark-blue during reaction with hydrogen. In the case of  $\text{WO}_3/\text{MoO}_3\text{-Pd}$ , the initial transmittance was similar to that of  $\text{MoO}_3\text{-Pd}$  in all wavelength ranges, but the rate of change after exposure to 4 %  $\text{H}_2$  for 1 minute showed a rapid response similar to that of  $\text{WO}_3\text{-Pd}$ . However, the transmittance change after the reaction appeared in a convex form at a short wavelength but the transmittance at the long wavelength range was higher than the short wavelength range. To confirm the reaction rates of those sensors, a time-series of transmittance changes were measured at a fixed wavelength of 700 nm, as shown in Fig. 5(d-f). Here,  $\text{MoO}_3\text{-Pd}$  showed a slower reaction rate compared to  $\text{WO}_3\text{-Pd}$  when exposed to 4 %  $\text{H}_2$ , but it exhibited an irreversible reaction where the changed transmittance was maintained even after hydrogen gas was purged. On the other hand,  $\text{WO}_3\text{-Pd}$  when exposed to hydrogen showed a rapid reaction rate and a reversible reaction, which means it quickly recovered to its original state after hydrogen gas was purged. Consequently, it is expected that the reversibility and reaction rate of the response are correlated. As for  $\text{WO}_3/\text{MoO}_3\text{-Pd}$ , it exhibited an irreversible state even after hydrogen removal, and although it was slower than  $\text{WO}_3$ , it achieved a reaction rate more than twice as fast as  $\text{MoO}_3\text{-Pd}$ .

In Fig. 6(a), measurements were performed at 0.1 %, 4 %, and 10 %  $\text{H}_2$  levels under  $\text{N}_2$  balance to investigate the reaction rate of  $\text{WO}_3/\text{MoO}_3\text{-Pd}$  at various  $\text{H}_2$  concentrations. Here, a set of three (3) samples from the same batch were taken to measure their response towards three different concentrations (i.e., 0.1 %, 4 %, and 10 %) of  $\text{H}_2$  gas exposure. For each sample, the  $\text{H}_2$  exposure test involved 30 seconds of 100 %  $\text{N}_2$  injection, followed by 5 minutes of  $\text{H}_2$  exposure, and finally, 100 %  $\text{N}_2$  injection again (i.e., purging). At 0.1 %  $\text{H}_2$  concentration, the  $\text{WO}_3/\text{MoO}_3\text{-Pd}$  sensor required a long response time of ca. 5 min to reach saturation point of response curve, i.e., exhibited a relatively slow reaction rate, indicating a limited response to low  $\text{H}_2$  concentrations. It should be noted that at a lower concentration than that of 0.1 %  $\text{H}_2$  gas, i.e., at ppm level, the reaction rate is extremely slow that cannot make significant visible color change even after long exposure time. It is not applicable in the context of visible/eye-readable gasochromic sensor and thus the concentration of 0.1 %  $\text{H}_2$  is determined as the limit of detection (LOD) of our proposed sensor. Nevertheless, the time-

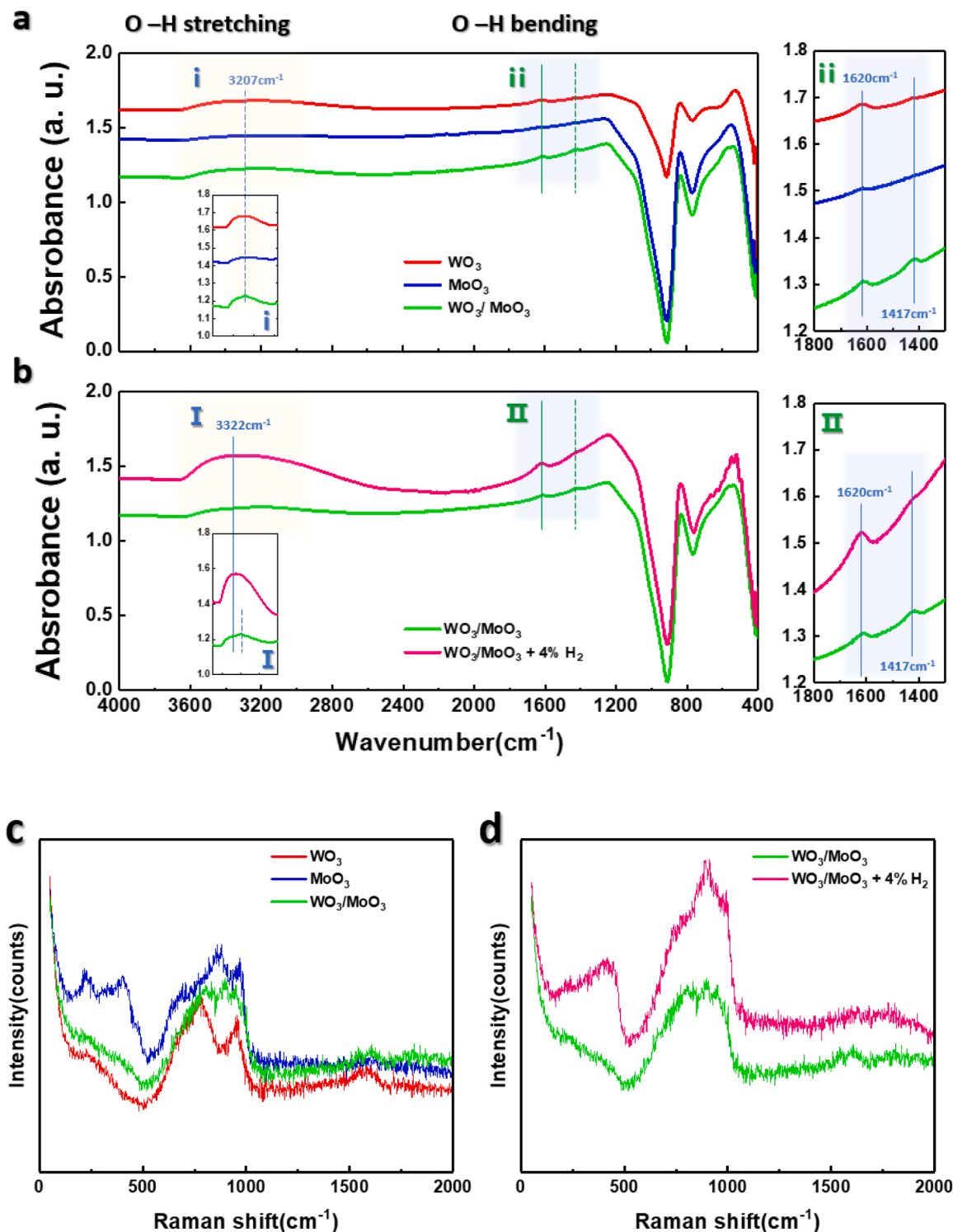


**Fig. 4.** Bonding properties of  $\text{WO}_3$ -Pd,  $\text{MoO}_3$ -Pd,  $\text{WO}_3/\text{MoO}_3$ -Pd film. (a) FT-IR spectra of three oxide films (i.e.,  $\text{WO}_3$ -Pd,  $\text{MoO}_3$ -Pd, and  $\text{WO}_3/\text{MoO}_3$ -Pd). (b) Comparing the FT-IR spectra of the  $\text{WO}_3/\text{MoO}_3$ -Pd film before and after exposure to 4 %  $\text{H}_2$ . (c) Raman spectra of those oxide samples. (d) Comparing the Raman spectra of the  $\text{WO}_3/\text{MoO}_3$ -Pd film before and after exposure to 4 %  $\text{H}_2$ , respectively.

dependent transmittance changes were observed to be moderate, suggesting a gradual and sustained reaction process. This slower reaction can be attributed to the restricted availability of hydrogen molecules for interaction with the sensor surface. At 4 %  $\text{H}_2$  concentration, the  $\text{WO}_3/\text{MoO}_3$ -Pd sensor showed a significantly rapid reaction rate, having a sensing speed (response time) of ca. 3.5 min. The time-dependent transmittance changes were substantial, indicating a strong response

to increasing hydrogen concentration. This accelerated reaction was facilitated by the high availability of hydrogen molecules, leading to more frequent and efficient interactions with the sensor surface. The sensor rapidly changed its color from gray to dark blue. At 10 %  $\text{H}_2$  concentration, the  $\text{WO}_3/\text{MoO}_3$ -Pd sensor exhibited faster transmittance changes (having a sensing speed of ca. 3 min) compared to the 4 %  $\text{H}_2$  concentration, reaching a lower level of maximum transmittance change

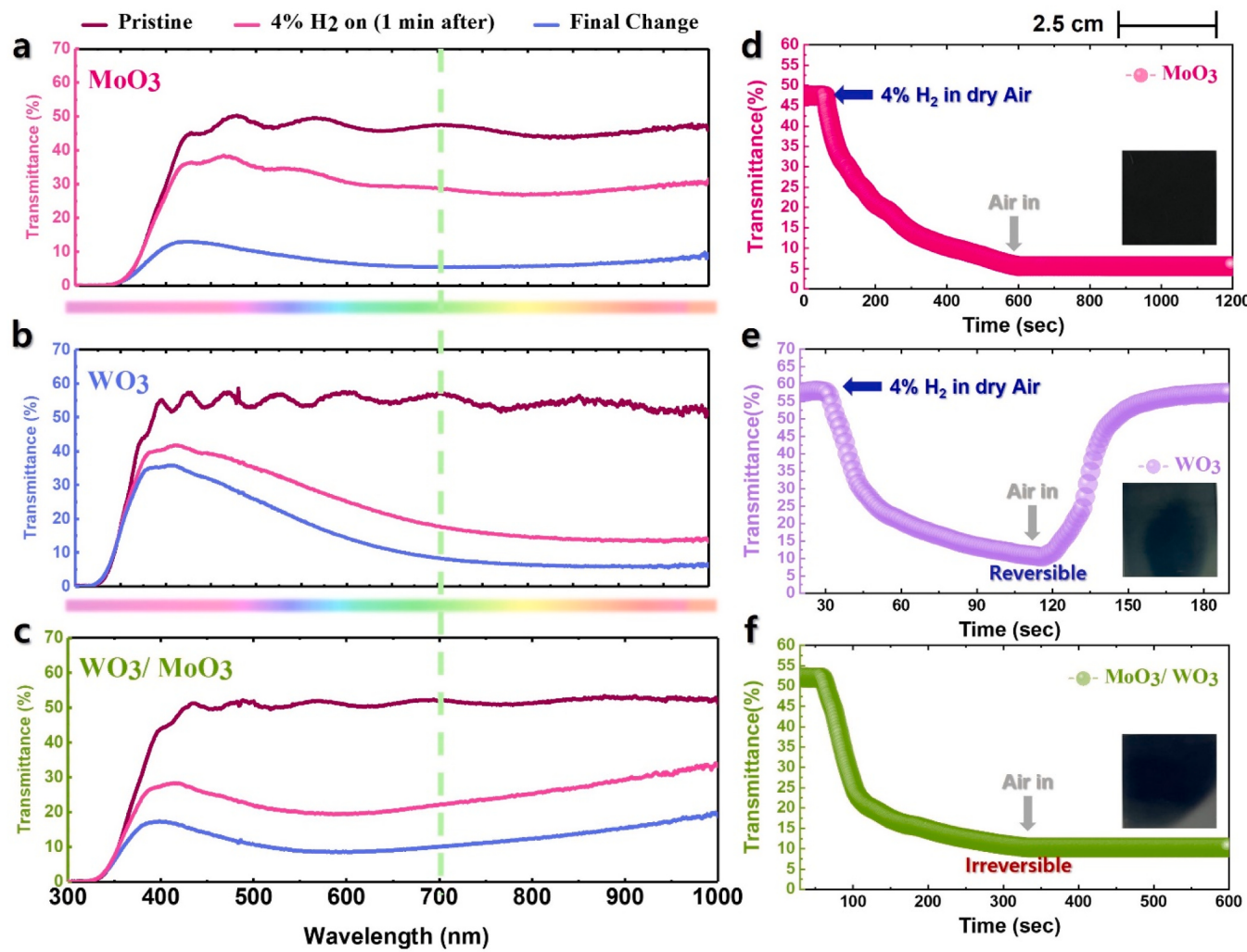


**Fig. 5.** UV-Vis spectrum of WO<sub>3</sub>-Pd, MoO<sub>3</sub>-Pd, WO<sub>3</sub>/MoO<sub>3</sub>-Pd film. (a, b, c) Transmittance change of MoO<sub>3</sub>-Pd, WO<sub>3</sub>-Pd, and WO<sub>3</sub>/MoO<sub>3</sub>-Pd film by UV-Vis spectroscopy with 1 minute and final change under 4 % H<sub>2</sub>/96 % N<sub>2</sub> gas conditions (d, e, f) Transmittance change over time for 4 % H<sub>2</sub> for MoO<sub>3</sub>-Pd, WO<sub>3</sub>-Pd, and WO<sub>3</sub>/MoO<sub>3</sub>-Pd film, respectively.

than the saturation point observed at 4 %. These results demonstrate that an increase in hydrogen concentration resulted in a more rapid decrease in the final transmittance and a change in the final color difference. The hydrogen detection capability of the WO<sub>3</sub>/MoO<sub>3</sub>-Pd sensor and its sensitivity to hydrogen concentration showed interrelated behaviors.

Furthermore, to quantitatively analyze the color difference, the color difference method ( $\Delta E$ ) was utilized as shown in [Figure S2 \(in Supplementary Information\)](#). The color difference ( $\Delta E$ ) of MoO<sub>3</sub>-Pd was measured to be 61.31, with small changes in the red-green axis (x) or yellow-blue axis (y), and changes mainly in brightness (z), from initial gray to dark gray. However, for WO<sub>3</sub>-Pd, a significant color shift was observed, transforming from an initial gray hue to a distinct blue color with a  $\Delta E$  value of 53.64. In the case of WO<sub>3</sub>/MoO<sub>3</sub>-Pd, the thin films exhibited a remarkable change, transitioning from an initial gray color to a dark bluish shade with a hint of violet, resulting in the highest  $\Delta E$  value of 64.90 among all the tested sensor samples. These results provide crucial information for quantitatively assessing the characteristics and changes of each sensor upon hydrogen exposure. The quantification of color changes using  $\Delta E$  enables a systematic evaluation of the sensors' response to hydrogen exposure, which is of significant importance for practical applications of WO<sub>3</sub>/MoO<sub>3</sub>-Pd thin films as visible hydrogen sensors. [Fig. 6\(b\)](#) shows the  $\Delta E$  retention results of WO<sub>3</sub>/MoO<sub>3</sub>-Pd in air i.e., ambient condition. From the  $\Delta E$  at 64.90 right after exposure to 4 %

H<sub>2</sub>, the WO<sub>3</sub>/MoO<sub>3</sub>-Pd sensor maintained 61.82 after 1 day and 56.75 after 5 days and showed a change of 51.51 after 14 days in air, confirming its irreversible characteristics. Nevertheless, completely irreversible sensors come with a limitation of reusability. In spite of the irreversible characteristics of our proposed sensor, its  $\Delta E$  retention tendency (with long time exposure to the environmental air) indicates the possibility of being reusable. To confirm this, we performed the repeatability test for two (2) consecutive cycles as shown in [Figure S4 \(in Supplementary Information\)](#). Here, a H<sub>2</sub> exposed sample (having a  $\Delta E$  value of 64.90) was kept at air environment condition and  $\Delta E$  values of the sample were recorded every other day for a week (i.e., 7 days). After a cycle of one week, the  $\Delta E$  value of the sample decreased from 64.90 (day 1 – 1st cycle) to 55.14 (day 7 – 1st cycle). The sample was then re-exposed to H<sub>2</sub> gas and a similar  $\Delta E$  measurements were repeated for the 2nd cycle. As found in the 2nd cycle, the sample was measured to exhibit a  $\Delta E$  value of 68.13 (day 1 – 2nd cycle) upon H<sub>2</sub> re-exposure and that of decreased to value of 58.04 (day 7 – 2nd cycle). These two repeatable cycles exhibit a similar trend in  $\Delta E$  retention, which indicates that the sensor might be reused after special treatment by exposing air at high flow rate for long time, which we would like to investigate in our future study.

To evaluate the selectivity of the WO<sub>3</sub>/MoO<sub>3</sub>-Pd sensor to noise gases, [Fig. 6\(c\)](#) compares the color change of the sensor to NH<sub>3</sub> (10 %), NO (1000 ppm), CH<sub>4</sub> (10 %), CO (1000 ppm), NO<sub>2</sub> (1000 ppm), CO<sub>2</sub>

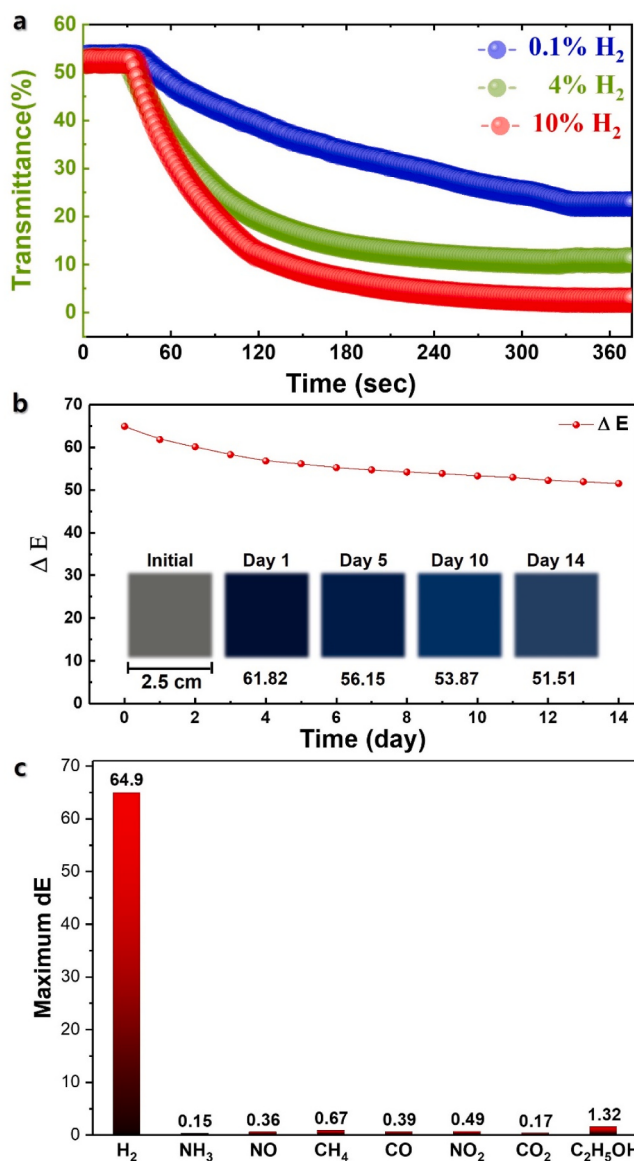


**Fig. 6.** Hydrogen sensing of WO<sub>3</sub>/MoO<sub>3</sub>-Pd (a) Transmittance changes with time according to hydrogen concentration (0.1 %, 4 %, 10 %) of WO<sub>3</sub>/MoO<sub>3</sub>-Pd sensors. (b) ΔE retention after 4 % hydrogen exposure (Initial, Day 1, Day 5, Day 10, Day 14) (c) Noise gas selectivity test of WO<sub>3</sub>/MoO<sub>3</sub>-Pd sensor.

(1000 ppm), and C<sub>2</sub>H<sub>5</sub>OH (10 %) gases. The color difference between the initial state and the exposed state showed a high variation of 64.9 for hydrogen gas, while it was measured as 0.15, 0.36, 0.67, 0.39, 0.49, 0.17, and 1.32 for NH<sub>3</sub>, NO, CH<sub>4</sub>, CO, NO<sub>2</sub>, CO<sub>2</sub>, and C<sub>2</sub>H<sub>5</sub>OH, respectively. The WO<sub>3</sub>/MoO<sub>3</sub>-Pd sensor exhibited color changes toward hydrogen gas significantly higher than toward other gases. This indicates that the sensor has a stronger reactivity to hydrogen. On the other hand, relatively low color differences were observed for NH<sub>3</sub>, NO, CH<sub>4</sub>, CO, NO<sub>2</sub>, CO<sub>2</sub>, and C<sub>2</sub>H<sub>5</sub>OH indicating that the WO<sub>3</sub>/MoO<sub>3</sub>-Pd sensor has relatively lower reactivity toward these gases and exhibits good selectivity to H<sub>2</sub> gas. The differences in color changes can be explained by the gas detection mechanisms of the WO<sub>3</sub>/MoO<sub>3</sub>-Pd sensor. In particular, hydrogen gas induces significant chemical reactions on the sensor surface, resulting in substantial color changes both at the surface and in the bulk by hydrogen atom diffusion. On the other hand, NH<sub>3</sub>, NO, CH<sub>4</sub>, CO, NO<sub>2</sub>, CO<sub>2</sub>, and C<sub>2</sub>H<sub>5</sub>OH may involve different interaction mechanisms that lead to relatively smaller color changes. This confirms the superior selectivity of the WO<sub>3</sub>/MoO<sub>3</sub>-Pd sensor toward hydrogen.

Further tests were performed to investigate the temperature and humidity effects on sensor responses, as shown in Figure S3 (in Supplementary Information). To investigate the temperature effects, a set of three (3) samples from the same batch were taken and sequentially exposed to 4 % H<sub>2</sub> gas at different temperatures i.e., 25, 50 and, 100 °C, respectively. The normalized transmittance of the sensor was measured after maintaining the temperature on a hot plate for 15 minutes at each temperature, as shown in Figure S3a (in Supplementary Information). Using the transmittance change at 25 °C as the reference value of 1, it was found that the normalized transmittance was 0.845 at 50°C and 0.577 at 100°C, showing a decreasing trend with increasing temperature. There are two models that explain the degradation in color: (1) for thermal annealing effect, a grain growth might lead to diminish a grain boundary diffusion of protons, and (2) surface water molecules providing channel of oxygen vacancy are evaporated and cavities from the absence of H<sub>2</sub>O are covered with some oxygen [9]. To investigate the effect of humidity on the sensing response, a set of four (4) samples from the same batch were taken and humid H<sub>2</sub> flow was introduced at various relative humidity values (i.e., 15, 40, 60 and 80 % RH, respectively) using a bubbler. As shown in Figure S3b (in Supplementary Information), using the transmittance change at 15 % RH as the reference value of 1, it was found that the transmittance was 0.676 at 40 % RH, 0.56 at 60 % RH, and 0.824 at 80 % RH, showing a decreasing trend with increasing relative humidity upto 60 % RH and that of increased at the relative humidity value of 80 % RH. As the relative humidity increases, the number of H<sub>2</sub>O molecules on the WO<sub>3</sub>/MoO<sub>3</sub>-Pd surface increases, interfering with the actual coloration process that occurs by the adsorption and dissociation of [H] atoms on the Pd surface due to the spill-over effect [44], [9]. Nevertheless, the presence of excessive humidity, i.e., 80 % RH, inside the gas chamber may initiate water protonation that can reduce the rate of interference in the coloration process. Therefore, the phenomenon of sudden increase in transmittance value at 80 % RH seems to occur due the water protonation effect [9].

### 3.3. DFT Results

To assess the reactivity of the WO<sub>3</sub>/MoO<sub>3</sub>-Pd sensor towards hydrogen, hydrogen atoms were randomly introduced into the amorphous cell. Each hydrogen atom within the sensor material was treated as an extrinsic interstitial defect. The formation energy calculation for these defects was carried out using the method outlined by Broberg et al. [52]. The defect formation energy ( $E^f[X^q]$ ) can be expressed as follows:

$$E^f[X^q] = E_{\text{tot}}[X^q] - E_{\text{tot}}[\text{bulk}] - \sum_i n_i \mu_i \quad (3)$$

Here, ( $E^f[X^q]$ ) and  $E_{\text{tot}}[\text{bulk}]$  denote the total energies obtained from density functional theory (DFT) calculations for supercells containing defects and defect-free configurations, respectively. The parameter represents the count of atoms introduced or extracted within the system. The expression  $\mu_i = \mu_i^{\text{ref}} + kT \ln \frac{P}{P_0}$  represents the chemical potential of hydrogen atoms with ideal gas assumption, where  $P$  and  $P_0$  denote the actual and reference pressures, respectively. The condition of  $\frac{P}{P_0} = 0.04$  was chosen from our experimental state to simulate a hydrogen gas concentration of 4 % in air.

Fig. 7(a) shows the atomic structure of amorphous W<sub>x</sub>Mo<sub>1-x</sub>O<sub>6</sub> employed in this DFT calculation, along with the H<sub>i</sub> formation energy as a function of Mo fraction. To assess the effect of the Mo fraction, we employed the average value of the H<sub>i</sub> formation energy in the amorphous W<sub>x</sub>Mo<sub>1-x</sub>O<sub>6</sub> ensemble structures [53]. As depicted in Fig. 7(b), the Mo fraction shows a notable trend in hydrogen dissolution. Below the critical Mo fraction of 0.215 – characterized by positive formation energy – the process of hydrogen dissolution is endothermic, inferring the potential for reversible hydrogen removal through external interventions. In contrast, exceeding this Mo fraction threshold of 0.215 in the W<sub>x</sub>Mo<sub>1-x</sub>O<sub>6</sub> sensor, the average H<sub>i</sub> formation energy is shifted to a

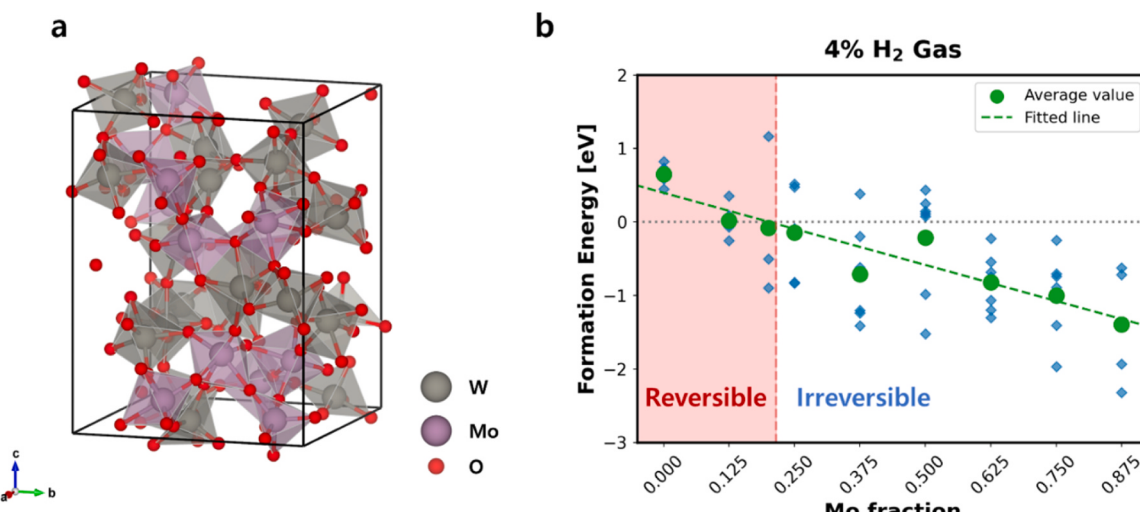


**Fig. 7.** (a) The atomic structure of amorphous W-Mo-O cell. (b)  $H_i$  formation energy as a function of the fraction of Mo in the W-Mo-O system.

negative value. This transition means spontaneous and sustained dissolution of hydrogen atoms in the oxide matrix, manifesting a state where the hydrogen atoms remain integrated within the structure. Consequently, it implies that once hydrogen is detected, the sensor could potentially sustain a degree of discoloration even as the hydrogen concentrations in the surrounding environment recede. This result explains the observed retention of discoloration in our experimental samples, characterized by a 2:1 W to Mo ratio.

#### 4. Conclusion

In conclusion, this study successfully developed an irreversible sensor with a fast response rate by properly mixing reversible and irreversible behaviors based on the  $\text{WO}_3/\text{MoO}_3\text{-Pd}$  thin film. The sensor was fabricated using a simple vacuum deposition procedure using RF magnetron sputtering and e-beam evaporation. It has been shown that the sensor has a vertically grown structure with a porous surface, which enhances the sensitivity of the sensor by promoting hydrogen adsorption and reactivity. X-ray photoelectron spectroscopy (XPS) measurements provided valuable insight into the chemical state of the films under hydrogen exposure. FT-IR and Raman measurements supported the presence of bound water molecules and further corroborated the XPS results. Gas sensing measurements demonstrated the color change of the film upon exposure to hydrogen, and the  $\text{WO}_3/\text{MoO}_3\text{-Pd}$  sensor obtained a faster response rate than the  $\text{MoO}_3\text{-Pd}$  and a higher  $\Delta E$  value than the  $\text{WO}_3\text{-Pd}$ . It was also theoretically verified that spontaneous and sustained dissolution of hydrogen atoms in the oxide matrix occurred by combining Mo to  $\text{WO}_3$  through DFT calculation. Finally, our material combination has shown potential opportunities for future hydrogen economy applications with the development of practical sensors.

#### CRediT authorship contribution statement

**ChiwanPark:** Writing – original draft, Methodology, Data curation. **Seung-IkHan:** Software, Formal analysis. **Le Thai Duy:** Writing – original draft, Investigation, Formal analysis. **Rubaya Yeasmin:** Writing – review & editing, Visualization, Formal analysis. **Gwanggyo Jung:** Software, Data curation. Dong Won Jeon: Investigation. Woongchan Kim: Investigation. Sung Beom Cho: Investigation. Hyungtak Seo: Writing – review & editing, Validation, Supervision, Resources, Project administration, Investigation, Funding acquisition, Conceptualization.

#### Declaration of Competing Interest

The authors declare that they have no known competing financial interests or personal relationships that could have appeared to influence the work reported in this paper.

#### Acknowledgements

This work was supported by the Commercialization Promotion Agency for R&D Outcomes (Project No: RS-2023-00282104) funded by the Ministry of Science and ICT, Republic of Korea.

#### Appendix A. Supporting information

Supplementary data associated with this article can be found in the online version at [doi:10.1016/j.snb.2024.137030](https://doi.org/10.1016/j.snb.2024.137030).

#### Data availability

Data will be made available on request.

#### References

- [1] T. Hübner, L. Boon-Brett, G. Black, U. Banach, Hydrogen sensors – a review, *Sens. Actuators B Chem.* 157 (2011) 329–352, <https://doi.org/10.1016/J.SNB.2011.04.070>.
- [2] C.H. Han, D.W. Hong, S.D. Han, J. Gwak, K.C. Singh, Catalytic combustion type hydrogen gas sensor using  $\text{TiO}_2$  and UV-LED, *Sens. Actuators B Chem.* 125 (2007) 224–228, <https://doi.org/10.1016/J.SNB.2007.02.017>.
- [3] I. Ivanov, A.M. Baranov, S. Akbari, S. Mironov, E. Karpova, Methodology for estimating potential explosion hazard of hydrocarbon with hydrogen mixtures without identifying gas composition, *Sens. Actuators B Chem.* 293 (2019) 273–280, <https://doi.org/10.1016/J.SNB.2019.05.001>.
- [4] D.V. Del Orbe, H. Yang, I. Cho, J. Park, J. Choi, S.W. Han, I. Park, Low-power thermocatalytic hydrogen sensor based on electrodeposited cauliflower-like nanostructured Pt black, *Sens. Actuators B Chem.* 329 (2021) 129129, <https://doi.org/10.1016/J.SNB.2020.129129>.
- [5] N.N. Samotaev, A.A. Vasiliev, B.I. Podlepetsky, A.V. Sokolov, A.V. Pisliakov, The mechanism of the formation of selective response of semiconductor gas sensor in mixture of  $\text{CH}_4/\text{H}_2/\text{CO}$  with air, *Sens. Actuators B Chem.* 127 (2007) 242–247, <https://doi.org/10.1016/J.SNB.2007.07.022>.
- [6] Y.A. Dobrovols'kii, L.S. Leonova, A.E. Ukshe, A.V. Levchenko, A.M. Baranov, A.A. Vasil'Ev, Portable sensors for hydrogen analysis, *Russ. J. Gen. Chem.* 77 (2007) 797–806, <https://doi.org/10.1134/S107036320704041X/METRICS>.
- [7] Y.A. Lee, L.T. Duy, S. Han, H. An, J. Park, R. Singh, H.Y. Kim, H. Seo, Confined interfacial alloying of multilayered Pd-Ni nanocatalyst for widening hydrogen detection capacity, *Sens. Actuators B Chem.* 330 (2021) 129378, <https://doi.org/10.1016/J.SNB.2020.129378>.
- [8] Z. Li, Z.J. Yao, A.A. Haidry, T. Plecenik, L.J. Xie, L.C. Sun, Q. Fatima, Resistive-type hydrogen gas sensor based on  $\text{TiO}_2$ : a review, *Int. J. Hydrog. Energy* 43 (2018) 21114–21132, <https://doi.org/10.1016/J.IJHYDENE.2018.09.051>.

- [9] L.T. Duy, R. Yeasmin, S.-I. Han, S. Iqbal, C. Park, H. Seo, Chemiresistive hydrogen sensors using a Pd-Ni nanocatalyst and a TiO<sub>x</sub>/PTFE humidity passivation, *Sens Actuators B Chem.* 394 (2023) 134387, <https://doi.org/10.1016/j.snb.2023.134387>.
- [10] S.-I. Han, R. Yeasmin, L.T. Duy, Y.-G. Noh, S.Y. Lee, C. Park, G. Jung, K.-S. Kwon, H. Seo, Inkjet printing Mo<sub>2</sub> nanosheets for hydrogen sensing applications, *J. Korean Ceram. Soc.* (2024), <https://doi.org/10.1007/s43207-024-00380-2>.
- [11] Y.A. Lee, S.S. Kalanur, G. Shim, J. Park, H. Seo, Highly sensitive gasochromic H<sub>2</sub> sensing by nano-columnar WO<sub>3</sub>-Pd films with surface moisture, *Sens Actuators B Chem.* 238 (2017) 111–119, <https://doi.org/10.1016/J.SNB.2016.07.058>.
- [12] W.J. Buttner, M.B. Post, R. Burgess, C. Rivkin, An overview of hydrogen safety sensors and requirements, *Int. J. Hydrog. Energy* 36 (2011) 2462–2470, <https://doi.org/10.1016/J.IJHYDENE.2010.04.176>.
- [13] P.P. Edwards, V.L. Kuznetsov, W.I.F. David, N.P. Brandon, Hydrogen and fuel cells: towards a sustainable energy future, *Energy Policy* 36 (2008) 4356–4362, <https://doi.org/10.1016/J.ENPOL.2008.09.036>.
- [14] Z. Wang, Y. Hu, W. Wang, X. Zhang, B. Wang, H. Tian, Y. Wang, J. Guan, H. Gu, Fast and highly-sensitive hydrogen sensing of Nb<sub>2</sub>O<sub>5</sub> nanowires at room temperature, *Int. J. Hydrog. Energy* 37 (2012) 4526–4532, <https://doi.org/10.1016/J.IJHYDENE.2011.12.004>.
- [15] N. Liu, M.L. Tang, M. Hentschel, H. Giessen, A.P. Alivisatos, Nanoantenna-enhanced gas sensing in a single tailored nanofocus, *Nat. Mater.* 2011 10 8 (10) (2011) 631–636, <https://doi.org/10.1038/nmat3029>.
- [16] Y.A. Lee, S.I. Han, H. Rhee, H. Seo, Correlation between excited d-orbital electron lifetime in polaron dynamics and coloration of WO<sub>3</sub> upon ultraviolet exposure, *Appl. Surf. Sci.* 440 (2018) 1244–1251, <https://doi.org/10.1016/J.APSUSC.2018.01.157>.
- [17] R. Yeasmin, L.T. Duy, S. Han, C. Park, H. Seo, High performing chemochromic hydrogen gas sensing using PVP encapsulated Pd: WO<sub>3</sub> nanocomposites, *Sens Actuators B Chem.* 394 (2023) 134416, <https://doi.org/10.1016/j.snb.2023.134416>.
- [18] S.-I. Han, M. Kumar, L.T. Duy, R. Yeasmin, C. Park, G. Jung, H. Kim, A.S. Khan, H. Dang, H. Seo, Effect of structural changes of Pd/WO<sub>3</sub> thin films on response direction and rate in hydrogen detection, *Sens Actuators B Chem.* 404 (2024) 135259, <https://doi.org/10.1016/j.snb.2023.135259>.
- [19] R. Yeasmin, H. Seo, Preparation of PVP Encapsulated Pd: WO<sub>3</sub> Nanocomposites for H<sub>2</sub> Gas Sensing, *IEEE Sens* 2023 (2023) 1–4. (<https://api.semanticscholar.org/CorpusID:265500046>).
- [20] R. Yeasmin, G. Jung, S. Han, C. Park, H. Seo, Self-healing and self-adhesive hydrogen gas sensing tape for robust applications (<https://doi.org/>), *Chem. Eng. J.* 482 (2024) 148911, <https://doi.org/10.1016/j.cej.2024.148911>.
- [21] S.S. Kalanur, I.H. Yoo, H. Seo, Pd on Mo<sub>3</sub>O<sub>4</sub> nanoplates as small-polaron-resonant eye-readable gasochromic and electrical hydrogen sensor, *Sens Actuators B Chem.* 247 (2017) 357–365, <https://doi.org/10.1016/J.SNB.2017.03.033>.
- [22] S.I. Han, S.Y. Lee, L.T. Duy, H. Seo, Reversible gasochromic hydrogen sensing of mixed-phase MoO<sub>3</sub> with multi-layered Pt/Ni/Pt catalyst, *Int. J. Hydrog. Energy* 46 (2021) 33339–33348, <https://doi.org/10.1016/J.IJHYDENE.2021.07.091>.
- [23] M. Wang, K.J. Koski, Reversible chemochromic MoO<sub>3</sub> nanoribbons through zerovalent metal intercalation, *ACS Nano* 9 (2015) 3226–3233, [https://doi.org/10.1021/ACSNANO.5B000336 SUPPL\\_FILE/NN5B000336\\_SI\\_001.PDF](https://doi.org/10.1021/ACSNANO.5B000336 SUPPL_FILE/NN5B000336_SI_001.PDF).
- [24] R. Wang, X. Lu, L. Hao, W. Jiao, W. Liu, J. Zhang, F. Yuan, F. Yang, Enhanced and tunable photochromism of MoO<sub>3</sub>-butylamine organic-inorganic hybrid composites, *J. Mater. Chem. C. Mater.* 5 (2017) 427–433, <https://doi.org/10.1039/C6TC04993A>.
- [25] Z. Lei, X. Yang, J. Dong, X. Yi, Novel metastable hexagonal MoO<sub>3</sub> nanobelts: Synthesis, photochromic, and electrochromic properties, *Chem. Mater.* 21 (2009) 5681–5690, [https://doi.org/10.1021/CM9023887 SUPPL\\_FILE/CM9023887\\_SI\\_001.PDF](https://doi.org/10.1021/CM9023887 SUPPL_FILE/CM9023887_SI_001.PDF).
- [26] J.W. Byon, M. Bin Kim, M.H. Kim, S.Y. Kim, S.H. Lee, B.C. Lee, J.M. Baik, Electrothermally induced highly responsive and highly selective vanadium oxide hydrogen sensor based on metal-insulator transition, *J. Phys. Chem. C.* 116 (2012) 226–230, [https://doi.org/10.1021/JP2080989 SUPPL\\_FILE/JP2080989\\_SI\\_001.PDF](https://doi.org/10.1021/JP2080989 SUPPL_FILE/JP2080989_SI_001.PDF).
- [27] J.M. Baik, M.H. Kim, C. Larson, C.T. Yavuz, G.D. Stucky, A.M. Wodtke, M. Moskovits, Pd-Sensitized single vanadium oxide nanowires: highly responsive hydrogen sensing based on the metal-insulator transition, *Nano Lett.* 9 (2009) 3980–3984. ([https://doi.org/10.1021/NL902020T SUPPL\\_FILE/NL902020T\\_SI\\_001.PDF](https://doi.org/10.1021/NL902020T SUPPL_FILE/NL902020T_SI_001.PDF)).
- [28] S. Mao, H. Zhou, S. Wu, J. Yang, Z. Li, X. Wei, X. Wang, Z. Wang, J. Li, High performance hydrogen sensor based on Pd/TiO<sub>2</sub> composite film, *Int. J. Hydrog. Energy* 43 (2018) 22727–22732, <https://doi.org/10.1016/J.IJHYDENE.2018.10.094>.
- [29] E. Şennik, Z. Çolak, N. Kılıç, Z.Z. Öztürk, Synthesis of highly-ordered TiO<sub>2</sub> nanotubes for a hydrogen sensor, *Int. J. Hydrog. Energy* 35 (2010) 4420–4427, <https://doi.org/10.1016/J.IJHYDENE.2010.01.100>.
- [30] N. Mohajeri, A. T-Raissi, G. Bokerman, J.E. Captain, B.V. Peterson, M. Whitten, S. Trigwell, C. Berger, J. Brenner, TEM-XRD analysis of PdO particles on TiO<sub>2</sub> support for chemochromic detection of hydrogen, *Sens Actuators B Chem.* 144 (2010) 208–214, <https://doi.org/10.1016/J.SNB.2009.10.064>.
- [31] D. Gogova, L.K. Thomas, B. Camin, Comparative study of gasochromic and electrochromic effect in thermally evaporated tungsten oxide thin films, *Thin Solid Films* 517 (2009) 3326–3331, <https://doi.org/10.1016/J.TSF.2008.12.020>.
- [32] D. Di Yao, J.Z. Ou, K. Latham, S. Zhuiykov, A.P. O'Mullane, K. Kalantar-Zadeh, Electrodeposited  $\alpha$ - And  $\beta$ -phase MoO<sub>3</sub> films and investigation of their gasochromic properties, *Cryst. Growth Des.* 12 (2012) 1865–1870. ([https://doi.org/10.1021/CG201500B/ASSET/IMAGES/LARGE/CG-2011-01500B\\_0008.JPG](https://doi.org/10.1021/CG201500B/ASSET/IMAGES/LARGE/CG-2011-01500B_0008.JPG)).
- [33] Z. Han, J. Ren, J. Zhou, S. Zhang, Z. Zhang, L. Yang, C. Yin, Multilayer porous Pd-WO<sub>3</sub> composite thin films prepared by sol-gel process for hydrogen sensing, *Int. J. Hydrog. Energy* 45 (2020) 7223–7233, <https://doi.org/10.1016/J.IJHYDENE.2019.12.149>.
- [34] S.S. Kalanur, J. Heo, I.H. Yoo, H. Seo, 2-D WO<sub>3</sub> decorated with Pd for rapid gasochromic and electrical hydrogen sensing, *Int. J. Hydrog. Energy* 42 (2017) 16901–16908, <https://doi.org/10.1016/J.IJHYDENE.2017.05.172>.
- [35] Y.A. Lee, S.I. Han, H. Rhee, H. Seo, Correlation between excited d-orbital electron lifetime in polaron dynamics and coloration of WO<sub>3</sub> upon ultraviolet exposure, *Appl. Surf. Sci.* 440 (2018) 1244–1251, <https://doi.org/10.1016/J.APSUSC.2018.01.157>.
- [36] G. Kresse, J. Furthmüller, Efficient iterative schemes for *ab initio* total-energy calculations using a plane-wave basis set, *Phys. Rev. B* 54 (1996) 11169, <https://doi.org/10.1103/PhysRevB.54.11169>.
- [37] P.E. Blochl, Projector augmented-wave method, *Phys. Rev. B* 50 (1994) 17953, <https://doi.org/10.1103/PhysRevB.50.17953>.
- [38] J.P. Perdew, K. Burke, M. Ernzerhof, Generalized gradient approximation made simple, *Phys. Rev. Lett.* 77 (1996) 3865, <https://doi.org/10.1103/PhysRevLett.77.3865>.
- [39] A. Jain, S.P. Ong, G. Hautier, W. Chen, W.D. Richards, S. Dacek, S. Cholia, D. Gunter, D. Skinner, G. Ceder, K.A. Persson, Commentary: the materials project: A materials genome approach to accelerating materials innovation, *APL Mater.* 1 (2013), <https://doi.org/10.1063/1.4812323/119685>.
- [40] V. Wang, N. Xu, J.C. Liu, G. Tang, W.T. Geng, VASPKIT: A user-friendly interface facilitating high-throughput computing and analysis using VASP code, *Comput. Phys. Commun.* 267 (2021) 108033, <https://doi.org/10.1016/J.CPC.2021.108033>.
- [41] B. Deng, P. Zhong, K.J. Jun, J. Riebesell, K. Han, C.J. Bartel, G. Ceder, CHGNet: pretrained universal neural network potential for charge-informed atomistic modeling, *Nat. Mach. Intell.* (2023), <https://doi.org/10.1038/s42256-023-00716-3>.
- [42] K. Kaur, C.V. Singh, Amorphous TiO<sub>2</sub> as a photocatalyst for hydrogen production: a DFT study of structural and electronic properties, *Energy Procedia* 29 (2012) 291–299, <https://doi.org/10.1016/J.EGYPRO.2012.09.035>.
- [43] J. Rino, N. Studart, Structural correlations in titanium dioxide, *Phys. Rev. B* 59 (1999) 6643, <https://doi.org/10.1103/PhysRevB.59.6643>.
- [44] L. Mai, F. Yang, Y. Zhao, X. Xu, L. Xu, B. Hu, Y. Luo, H. Liu, Molybdenum oxide nanowires: synthesis & properties, *Mater. Today* 14 (2011) 346–353, [https://doi.org/10.1016/S1369-7021\(11\)70165-1](https://doi.org/10.1016/S1369-7021(11)70165-1).
- [45] S.A. Aly, A.A. Akl, D.H. Mahmoud, Microstructural and electrical characteristics of sprayed tungsten oxide thin films, *Int. J. New. Horiz. Phys.* 2 (2015) 47–52.
- [46] S.K. Sen, T.C. Paul, S. Dutta, M.N. Hossain, M.N.H. Mia, XRD peak profile and optical properties analysis of Ag-doped h-MoO<sub>3</sub> nanorods synthesized via hydrothermal method, *J. Mater. Sci. Mater. Electron.* 31 (2020) 1768–1786, <https://doi.org/10.1007/s10854-019-02694-y>.
- [47] Y. Sun, L. Chen, Y. Wang, Z. Zhao, P. Li, W. Zhang, Y. Leprince-Wang, J. Hu, Synthesis of MoO<sub>3</sub>/WO<sub>3</sub> composite nanostructures for highly sensitive ethanol and acetone detection, *J. Mater. Sci.* 52 (2017) 1561–1572, <https://doi.org/10.1007/s10853-016-0450-2>.
- [48] J. Zhu, M. Vasilopoulou, D. Davazoglou, S. Kennou, A. Chroneos, U. Schwingenschlögl, Intrinsic defects and H doping in WO<sub>3</sub>, *Sci. Rep.* 7 (1) (2017) 1–9, <https://doi.org/10.1038/srep40882>.
- [49] T.H. Fleisch, G.J. Mains, An XPS study of the UV reduction and photochromism of MoO<sub>3</sub> and WO<sub>3</sub>, *J. Chem. Phys.* 76 (1982) 780–786, <https://doi.org/10.1063/1.443047>.
- [50] H. Habazaki, Y. Hayashi, H. Konno, Characterization of electrodeposited WO<sub>3</sub> films and its application to electrochemical wastewater treatment, *Electrochim. Acta* 47 (2002) 4181–4188, [https://doi.org/10.1016/S0013-4686\(02\)00435-8](https://doi.org/10.1016/S0013-4686(02)00435-8).
- [51] S.H. Lee, H.M. Cheong, P. Liu, D. Smith, C.E. Tracy, A. Mascarenhas, J. Roland Pitts, S.K. Deb, Raman spectroscopic studies of gasochromic a-WO<sub>3</sub> thin films, *Electrochim. Acta* 46 (2001) 1995–1999, [https://doi.org/10.1016/S0013-4686\(01\)00379-6](https://doi.org/10.1016/S0013-4686(01)00379-6).
- [52] D. Broberg, B. Medasani, N.E.R. Zimmermann, G. Yu, A. Canning, M. Haranczyk, M. Asta, G. Hautier, PyCDT: A Python toolkit for modeling point defects in semiconductors and insulators, *Comput. Phys. Commun.* 226 (2018) 165–179, <https://doi.org/10.1016/J.CPC.2018.01.004>.
- [53] G. Kang, D. Lee, K. Lee, J. Kim, S. Han, First-principles study on the negative-U behavior of K centers in amorphous Si<sub>3</sub>N<sub>4-x</sub>, *Phys. Rev. Appl.* 10 (2018) 064052, (<https://doi.org/10.1103/PHYSREVAPPLIED.10.064052/FIGURES/6/MEDIUM>).

**Chiwan Park** earned his bachelor's degree in 2022 from Department of Advanced Materials Engineering, University of Suwon, South Korea, and MS degree in 2024 from Ajou University. He earned a master's degree from the department of Energy Systems Research at Ajou University under Prof. H. Seo's group in February 2024. Currently, he researches and develops oxide semiconductors, metal-based hydrogen detection sensors.

**Seung-Ik Han** received his M.S./Ph.D. degree in 2023 from Ajou University and worked in Advanced Electronic & Energy Materials Laboratory (AEEM) and Engineering Research Institute of Ajou University until February 2024. He has served as a Postdoctoral researcher of Multifunctional Engineering Dynamics Automation Lab (MEDAL) of University of Calgary since March 2024 till now. His research interests are the fabrication and optimization of Metal-oxide semiconducting functional composite materials and gas sensor devices.

**Le Thai Duy** has worked with Prof. H. Seo's group at Ajou University after finishing the integrated M.S./Ph.D. program from Sungkyunkwan University in 2017. He was one of the selected candidates for KRF/BP Fellowship in 2018, funded by National Research Foundation of Korea. Currently, he is working as a faculty at Vietnam National University. His current research interest is the development of nanocatalyst and functional materials for wearable sensors and energy devices.

**Rubaya Yeasmin** received her B.Sc. Eng. degree in Applied Physics & Electronic Engineering from University of Rajshahi, Bangladesh in 2018, and the integrated MS & Ph.D. degree in Materials Science & Engineering from Ajou University in February 2024. Currently, she is working as a post-doctoral researcher with the department of Energy Systems Research, and Engineering Research Institute at Ajou University. Her research interests includes self-healing functional composites for multimodal sensing applications.

**Gwanggyo Jung** earned his bachelor's degree in 2023 from Department of Materials Science and Engineering, Ajou University, South Korea. He is pursuing a master's degree at Ajou University's Advanced Electronic Energy Materials Laboratory under Prof. H. Seo's team. Currently, he researches and develops multimodal hydrogen detection sensor and NIR fluorine detection optical sensor.

**Dong Won Jeon** earned his bachelor's degree in 2023 from Department of Materials Science and Engineering, Ajou University, South Korea. He is pursuing a master's degree at Ajou University's Materials Modeling Laboratory under Prof. S. Cho's team. His research focuses on the simulation and development of battery materials.

**Woongchan Kim** earned his bachelor's degree in 2023 from Department of Materials Science and Engineering, Ajou University, South Korea. He is pursuing a master's degree at Ajou University's Materials Modeling Laboratory under Prof. S. Cho's team. His research focuses on the simulation and development of defected structure.

**Sung Beom Cho** is an Assistant Professor at Ajou University, where he is building a research program in computational materials science and materials informatics. He earned his Ph.D. from Hanyang University (2017) and completed postdoctoral research at Washington University (2017–2018). As Senior Researcher at KICET (2018–2022), Cho supported industrial applications, particularly in electronic and energy systems, utilizing various computational tools. His research focuses on leveraging computational methods to understand and predict the behavior of various materials.

**Hyungtak Seo** received his Ph.D. degree in 2008 from North Carolina State University and worked in Lawrence Berkeley National Laboratory until September 2011. He has served as a professor of Ajou University since 2011 till now. His Advanced Electronic & Energy Materials laboratory (AEEM) is one of the top performance groups in Ajou University. His current interests are in (i) fabrication of nanomaterials for solar cells and photocatalysis applications; (ii) design of materials/devices for next generation ICs (resistive memory, logic), optoelectronic devices, flat panel displays; (iii) tuning nanoscale semiconductor electronic properties for electrical and energy applications; etc.